Telescopic Observations of Lunar Hydration: Variations and Abundance

C. I. Honniball[1,†], P. G. Lucey[1], C. M. Ferrari-Wong[1], A. Flom[1], S. Li[1], H. M. Kaluna[2] and D. Takir[3]

[1]Hawai'i Institute of Geophysics and Planetology, University of Hawai'i at Mānoa, Honolulu, HI, USA. [2]Department of Physics and Astronomy, University of Hawaii at Hilo, Hilo, HI, USA. [3]USGS to JETS/ARES, NASA JSC, Houston, TX, USA.

Corresponding author: Casey I. Honniball (casey.i.honniball@nasa.gov)

[†]Current Location: NASA Postdoctoral Program Fellow, NASA Goddard Space Flight Center, Greenbelt, MD, USA.

Key Points:

- New observations of the Moon from the NASA InfraRed Telescope Facility are used to investigate variations of hydration on the lunar surface
- Long wavelengths beyond 3 μm provide strong constraints for thermal corrections
- Variations in the lunar 3 μm hydration band are observed with latitude, time of day, and composition

Abstract

Prior to 2009, the Moon was believed to be anhydrous. However, observations by three spacecraft revealed a hydrated surface by reporting a 3 μm absorption band attributed to hydroxyl and possibly molecular water. The Moon Mineralogy Mapper (M^3) spectrometer, onboard the Chandrayaan-1 spacecraft is mainly used to study the lunar 3 μm band but its spectral range ends at 3 μm. The limited wavelength range of M^3 has allowed observed variations in the 3 μm band to be called into question due to uncertainties in thermal corrections.

To investigate the validity of variations in the lunar 3 μm band, we used the SpeX infrared spectrograph at the NASA InfraRed Telescope Facility at Maunakea Observatory in Hawai'i. With SpeX, we are able to obtain lunar data over a wavelength range of 1.67 to 4.2 μm at 1 – 2 km spatial resolution. The long wavelengths provide strong constraints on thermal emission corrections. We confirm that the 3 μm band varies with lunar time of day as well as with latitude and composition. Each observation reveals strong variations in abundances of hydroxyl and possibly molecular water. The data reveal a decrease in abundance with increasing lunar local time, an asymmetric trend about the equator that favors the southern latitudes, and higher concentrations in highland regions. The longer wavelengths provided by SpeX have allowed us to examine variations in the 3 μm band and provide definitive evidence that the variations are due to changes in hydration.

Plain Language Summary

Until recently, the Moon was thought to be dry. However, this view drastically shifted in 2009 when spacecraft observed a hydration feature. The spacecrafts observed the hydration feature varying with temperature on the Moon. However, due to uncertainties in correcting the data for emissions from the high temperature of the Moon, the variation of the hydration feature was called into question. To verify the variation of the hydration feature we obtained new observations of the Moon that provide strong constraints on thermal corrections using the NASA InfraRed Telescope Facility at Maunakea Observatory in Hawai'i. With this new data we find that the hydration feature on the Moon varies with temperature, latitude, and composition. The presence of variation shows that there are temperature driven processes occurring on the surface on the Moon.

1 Introduction

In 2009 a major discovery in lunar science was the report of a widespread hydration feature on the surface of the Moon. The hydration was observed by spectrometers on three different spacecraft, Chandrayaan-1, Deep Impact, and Cassini (Pieters et al., 2009; Sunshine et al., 2009; Clark, 2009). This hydration feature is in the 2.8 to 3.5 μm region (referred to as the "3 μm band") and is due to the presence of hydroxyl (OH) attached to a metal cation, or molecular water (H_2O), or a combination of the two. The discovery of the 3 μm band on the surface of the Moon was anticipated by several laboratory studies that observed OH in experiments simulating the production of OH from solar wind interactions with oxygen-rich materials (Hapke, 1965; Zeller et al., 1966; Zeller and Ronca, 1967). These studies showed that bombarding silicate glass materials (analogous to lunar regolith) with high-energy protons (analogous to solar wind) produces OH on the surface of grains and exhibit a 3 μm band (Zeller et al., 1966; Zeller and Ronca, 1967). This was later confirmed by more recent studies (Ichimura et al., 2012; Mattern et al., 1976; Siskind et al., 1977; Guermazi et al., 1987; Gruen et al., 1975; Bradley et al., 2014).

Variations of the 3 μm band intensity with temperature were reported using global spectral imaging of the Moon by the infrared High Resolution Imaging spectrometer on Deep Impact (Sunshine et al., 2009). From the spacecraft's distant vantage point during one of its two lunar flybys, the spectrometer captured global snapshots of the Moon. These data revealed a strong correlation between lunar surface temperature and the strength of the 3 μm band. The 3 μm region is complicated by the fact that it is a combination of solar reflected radiance and thermally emitted radiance (McCord et al., 2011). However, data from Deep Impact, despite the relatively low spatial resolution and limited time of day coverage, has the distinct advantage of including data near and beyond 4 μm where the spectrum is dominated by thermal emission enabling confident removal of this component. The thermally corrected Deep Impact spectra are highly likely to have detected strong variations in the abundance of total water (OH + H_2O) (Stolper, 1982; Starukhina, 2001; King et al., 2004; McIntosh et al., 2017) with lunar surface temperature. However, the data do not contain repeat coverage to definitively confirm diurnal variations.

Diurnal variations in the 3 μm band were also observed in data from the Chandrayaan-1 Moon Mineralogy Mapper (M^3) spectrometer that collected data from lunar polar orbit. Pieters et al. (2009) extended the Deep Impact temporal and spatial coverage using M^3 data and reported diurnal variations in the 3 μm band depth in repeat observations of the same locations. However, data from M^3 terminate at 3 μm, leaving little spectral range to validate corrections for thermal emission. Three groups have analyzed M^3 data applying subtly different thermal corrections and each arrive at strikingly different conclusions ranging from strong diurnal variation to no variation in 3 μm band intensity at all (Li and Milliken, 2017; Wölher et al., 2017; Grumpe et al., 2019; Bandfield et al., 2018). However, McCord et al. (2011) pointed out that observations of the lunar surface at wavelengths beyond 3 μm greatly improve the removal of thermal emission due to the sharply increasing thermal emission with wavelength and are strongly recommended to address the validity of variation in the 3 μm band.

In this paper we use ground-based infrared spectroscopy of the Moon from 1.67 μm to 4.2 μm to constrain our thermal correction. This new data set allows us to determine the degree of diurnal variation in 3 μm band with repeat observations of the same lunar locations. We quantify the total water abundance in our spectra and to compare these new estimates to previous spacecraft estimates. Observations were conducted at the NASA Infrared Telescope Facility (IRTF) at Maunakea Observatory, obtaining spatially resolved data (~1 to 2 km) covering most lunar times of day over 180˚ of latitude from pole-to-pole along the zero longitude meridian.

2 Data

We collected 3,395 spatially resolved spectra of the lunar surface with the IRTF SpeX spectrograph on 6 nights between January 17th 2019 and May 15th 2019. Data were acquired in the long-wavelength cross-dispersed mode called 'LXD Short' that produces spectra from 1.67 to 4.2 μm with a spectral resolution of R ~ 2500 (Rayner et al., 1998). We use the narrowest slit available, 0.3 x 15 arcsecond (about 0.6 x 30 km at the lunar center of disk), to limit saturation and integration times ranging from 0.5 to 2 seconds depending on the lunar illumination conditions. Occasional saturation is observed at wavelengths near 4 μm when the lunar surface is the warmest; for the few spectra where saturation occurs, this region is avoided in processing and interpretation. We define saturation as when the raw digital number counts are above 29,000. When saturation is observed data out to 3.6 μm still provides strong thermal constraints.

The observing goal was to acquire data for the same locations over a range of lunar times of day by taking advantages of the evolving lunar phase between observing nights. To maximize

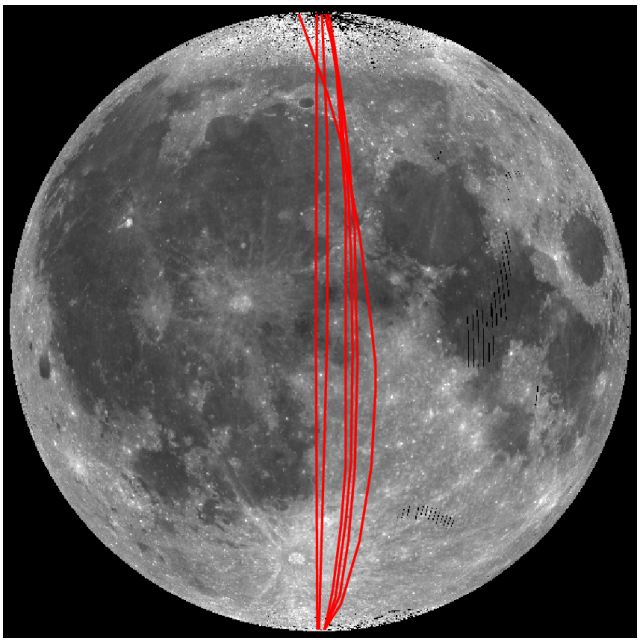

Figure 1: Image of the Moon with the location of lunar chord observations for this project.

diurnal and latitude coverage, we scanned the spectrometer slit across the Moon while reading out the SpeX detector. We conducted these scans with the slit oriented either perpendicular (in a push broom mapping fashion) or parallel (as a chord across the Moon) to the lunar meridian. After each detector readout, the slit is offset by 2 arcseconds per frame in the perpendicular mode or 7 arcseconds per frame (about half the slit length) in the parallel mode. The parallel orientation allows us to scan from one lunar pole to the other to create a spectral profile at 1 arcsecond intervals across the Moon. The offset rates of the scan is in both RA and DEC to produce scans near the zero longitude meridian. The parallel mode maximizes latitude and temperature coverage, producing data with near constant lunar time of day for a given observation. Table 1 summarizes the observations, and Figure 1 shows the location of each scan on the Moon.

Table 1: Information regarding the data acquired.

Date UTC	Lunar Local Time	# of Frames	Phase Angle	Integration Time (s)	Solar Analog Star	Slit Orientation
01-18-2019	09:11 - 09:33	990	40.3°	0.5	HD25680	Perpendicular
01-20-2019	10:23 - 11:29	1026	11.5°	0.5	HD25680	Perpendicular
03-27-2019	16:32 - 17:34	582	-84.1°	1	HD162255	Parallel
05-13-2019	07:04 - 07:49	275	74.0°	2	HD89010	Parallel
05-14-2019	07:57 - 08:37	268	60.7°	2	HD106423	Parallel
05-15-2019	08:47 - 08:54	254	47.1°	1	HD106423	Parallel

3 Methods

Data reduction includes flat-field correction, wavelength calibration, correction for stray light within the SpeX instrument, sky subtraction, telluric correction using solar analog stars, merging

of the several orders into single spectra, thermal emission correction, and conversion of reflectance data to water abundance.

3.1 SpeX data calibration

Standard flat-field and wavelength calibrations were conducted using the Spextool (V4.0) data reduction package (Cushing et al., 2004; Vaca et al., 2003) employing the internal flat-field and Ar lamp data obtained at the beginning and end of each night. Our SpeX data exhibit stray light from internal scattering within the spectrometer. When uncorrected, the stray light causes zero signal regions (due to atmospheric opacity) to have artificially elevated signals above zero. In Figure 2 the stray light manifests as a pedestal within the 2.5 - 2.8 μm region where the atmosphere is opaque which should result in zero signal after sky subtraction. Typical observations of stars and other point sources remove this stray light background through beam-switching, but this cannot be used for extended objects such as our lunar observations. The stray light can be seen in the raw data for one of the cross-dispersed orders in Figure 3. To remove the stray light we take advantage of a "background subtract" mode in Spextool which allows subtracting a wavelength dependent window within the slit from the rest of the data in the slit. Spextool does not allow background definition outside the slit where the stray light occurs, so we developed code to isolate the stray light just outside the slit image, and then shifted it to the ends of the slit where signal is low and are discarded in our processing (Figure 3). At this position Spextool can be instructed to subtract this portion of the slit where we have moved in stray light from the data. We then process the modified raw data with the stray light correction through Spextool as usual. An example of the effectiveness of the stray light correction is shown in Figure 2.

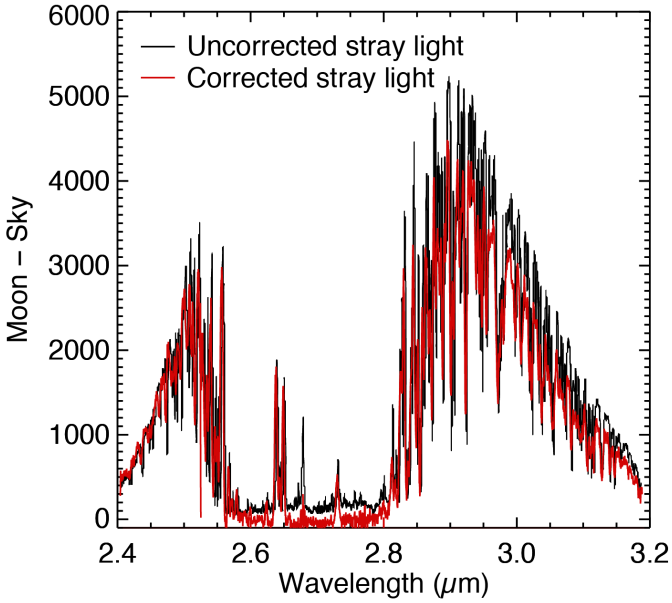

Figure 2: Example of the stray light correction in the opaque water region of the atmosphere from 2.5 to 2.8 μm. The black spectrum sits on a pedestal of stray light causing the band to appear to have signal. Data after stray light removal are shown in red and now has a mean value of zero as expected in a region that is opaque.

At this point, spectra from ten, 1 arcsecond windows along the slit are extracted from the spectral images using Spextool. Each order is extracted separately and then merged together to produce a single spectrum. Where orders overlap in wavelength, data from the order with the higher raw signal is included; lower signal redundant data is discarded.

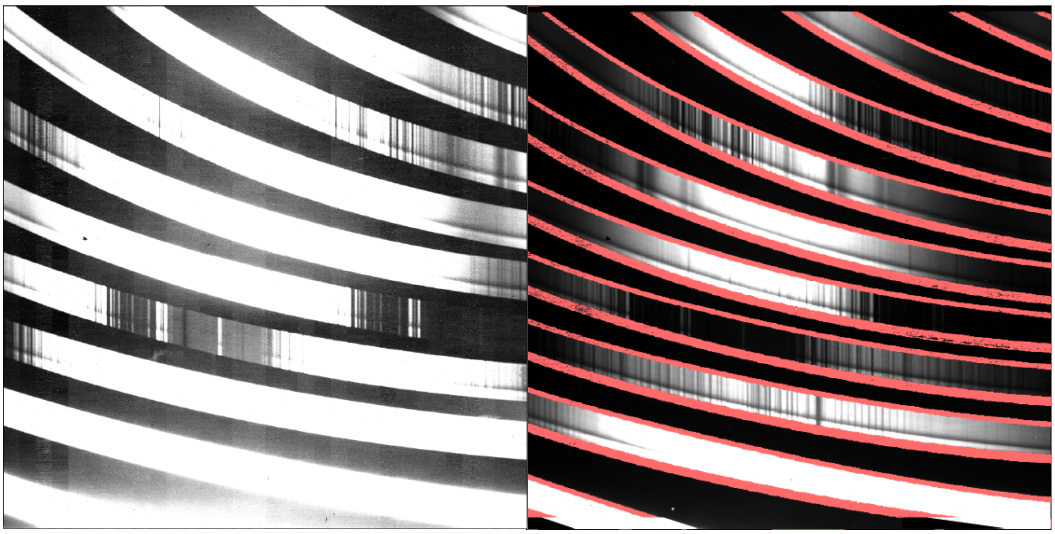

Figure 3: The bright stripes are the 7 crossed dispersed orders of SpeX. Stray light can be seen between the orders when the contrast of the image is enhanced (left). The red stripes on the right indicate where stray light was moved into each order.

Because the Moon is a very large extended object that does not permit chopping or nodding, removal of sky and telluric emission features require sole observations of the sky near the Moon to capture thermal background and sky emission. Observations of the sky are taken just off the limb of the Moon and are subtracted from the lunar spectra.

Throughout each night, small shifts in wavelength calibration occur from small displacements of spectrometer components at different orientations of the telescope. While these shifts are small with respect to the broad hydration feature of interest, the high resolution of SpeX results in large artifacts during star calibration near regions of abundant atmospheric spectral lines in the presence of spectral misregistration. Due to the large amount of data, we developed code to correct for wavelength shifts. In each order we found and applied subpixel shifts that minimized spectral ratios between the Moon and the solar analog star in spectral regions with dense concentrations of atmospheric lines. We apply these shifts to align the lunar data to the solar analog star used for extinction correction.

Finally, spectra are corrected for atmospheric transmission by normalizing the sky-subtracted lunar data to observations of solar analog stars. Stars are selected from solar analog stars used for asteroid observations with the IRTF (Takir and Emery, 2012). The solar analog spectrum is divided out from the sky corrected lunar data to remove atmospheric absorption lines and to correct for the solar spectral shape inherent to reflectance observations of planetary bodies. Figure 4 is an example of the final lunar spectrum. While we chose calibration stars from Takir and Emery (2012) that are close in proximity to the Moon with a similar airmass, some telluric absorptions are not fully removed due to differences in atmospheric conditions between the lunar observations and star observations. The solar analogs used for each observation are listed in Table 1.

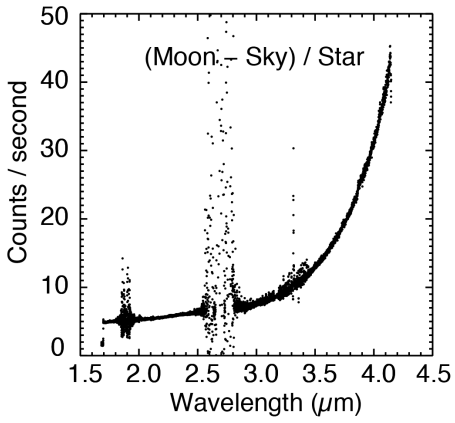

Figure 4: Example of a lunar spectrum after background sky emissions and telluric absorptions are corrected.

3.2 Removal of Thermal Emission

Lunar spectra longward of 2.5 μm are heavily affected by thermally emitted radiance. This thermal radiation is dependent on temperature, albedo, emissivity, surface roughness, and thermal inertia. As pointed out above, accurate removal of thermal emission is vital for investigation of the 3 μm feature and its variation. Ground-based observations of total water on asteroids has been conducted for over 40 years (Lebofsky, 1978) and asteroid spectra are also affected by thermal emission and methods are available for its correction. For this lunar work, we follow the methodology widely used for asteroid thermal emission removal defined by Rivkin et al. (2005), Reddy et al. (2009), and Takir and Emery (2012), in part because they also used SpeX for their asteroid observations and so this method is well established for that spectrometer.

Planetary astronomers observing in the visible and near infrared typically normalize their data to solar analog stars that have a spectral shape similar to the sun. This normalization produces astronomical spectra that are similar to spectra of samples with the same composition measured in the laboratory. However, at longer wavelengths such as used here, the thermal emission is obvious as a strong turn-up in the spectrum relative to the star at longer wavelengths (Figure 4). Rivkin et al. (2005) called this turn-up the "thermal excess" and used the Standard Thermal Model developed by Lebofskyet et al. (1986) to model this excess and remove it. Thermal excess (γ) is defined as:

$$\gamma = \frac{R_\lambda + T_\lambda}{R_\lambda} - 1, \quad (1)$$

where R_λ is the reflected spectral radiance (W/m^2/μm/sr) and T_λ is the thermal spectral radiance (W/m^2/μm/sr) of the target.

Rivkin et al. (2005) uses the observed data to determine a measured thermal excess ($\gamma_{measured}$), then fits this measured thermal excess with a modeled excess (γ_{model}) and subtracts the model from the spectrum with the goal of mitigating the thermal excess. For the measured lunar thermal excess, the numerator in the first term of Equation 1 ($R_\lambda + T_\lambda$) is the measured lunar spectrum normalized to the solar standard star at a standard wavelength (1.75 μm) ($R_{\frac{Moon}{star}}$). The R_λ in the denominator of the first term is a model reflectance estimated by fitting the data from 1.7 to 2.5 μm with a straight line and extrapolating to the longer wavelengths. In the lunar case strong pyroxene absorptions are usually observed in the 2 μm region, so our model reflectance is fit at 1.7 and 2.5 μm avoiding the pyroxene band (R_{con}). The measured thermal excess equation for the lunar case is therefore:

$$\gamma_{measured} = \frac{R_{\frac{Moon}{star}}}{R_{con}} - 1. \quad (2)$$

To obtain a purely reflectance spectrum of the Moon (R_{Moon}) we have to subtract a model of the measured thermal excess (γ_{model}):

$$R_{Moon} = R_{\frac{Moon}{star}} - \gamma_{model}. \quad (3)$$

In order to model the thermal excess (γ_{model}) we model both the expected lunar radiance (which includes solar radiance) and thermal radiance. The lunar radiance (L_{model}) is given in Equation 4:

$$L_{model} = \frac{I_{solar}}{\pi} * MI_{30,0,30} * R_{con} \ \ W/m\text{^}2/\mu m/sr \quad (4)$$

where I_{solar} is the solar irradiance [ASTM E490-00a, 2014] divided by π to convert it to units of radiance. $MI_{30,0,30}$ is the reflectance of the Moon at the location observed extracted from global albedo data collected by the Multiband Imager (MI) on the Kaguya spacecraft [Ohtake et al., 2008], corrected to our observing geometry from the standard photometric geometry of the data set

(incidence (i) = 30˚, emission (e) = 0˚, phase angle = 30˚). The data are converted from the standard geometry to that of our observations using the methods of Hapke (2012). The retrieval of the MI reflectance value uses the latitude and longitude at which each spectrum was acquired, and is resampled to our spatial resolution. Lastly, R_{con} is the modeled reflectance defined above.

3.3 Thermal model

Asteroid thermal corrections typically use an asteroid standard thermal model (Harris 1998). However, to speed up the calculations necessary for our large data set we use a simplified thermal model that assumes the lunar surface to be composed of two components (to account for surface roughness): a single temperature for the hot illuminated component in radiative equilibrium, and a single temperature for the cold shadowed component. Detailed thermal models show the shaded component to be very cold, typically less than 150K (Bandfield et al. 2015). The two component thermal model is defined as:

$$L = A\epsilon_1 B(T_1) + (1 - A)\epsilon_2 B(T_2), \quad (5)$$

where L is the model radiance, A is the area of the hot component (accounting for surface roughness), ϵ_1 is the emissivity of the hot component, and T_1 is its temperature, T_2 is the temperature of the cold component and ϵ_2 is its emissivity. In the spectral region less than 4 μm, emission from surfaces at cold temperatures (T_2) can be neglected, so the two component thermal model simplifies to:

$$L_{thermal} = A\epsilon B(T_1). \quad (6)$$

For the purposes of this model we assume an emissivity of 0.9 (Takir and Emery, 2012). Rather than iteratively fit $\gamma_{measured}$, we compute a large lookup table for $L_{thermal}$ varying A and T_1 with increments of 0.5% in A and 0.5 K for T_1.

Because lunar data are affected by thermal radiance at wavelengths shorter than 3 μm, the modeled reflectance (R_{con}) of the data near 2.4 μm includes some of the thermal component in the measured thermal excess. Due to this, the modeled thermal excess must be normalized at the same wavelengths as the data (C) before the thermal excess model can be used to find the correct thermal excess model for the data. The final modeled thermal excess is given by:

$$\gamma_{model} = \frac{\left(\frac{L_{model}+L_{thermal}}{L_{model}}\right)}{C} - 1. \quad (7)$$

With both the $\gamma_{measured}$ and the library of γ_{model}, we then subtract all thermal excess models from each the lunar $\gamma_{measured}$ and use the mean of the absolute value of the difference to determine the best fit. The model that provides the minimum value is chosen as the best fit γ_{model}. If saturation occurs at the longest wavelengths in the data then the best fit thermal excess model is defined out to 3.6 μm which still allows for strong thermal constrains beyond 3 μm. If no saturation is observed, the best fit thermal model is defined out to 4 μm. Figure 5 shows an example of a high latitude spectrum and the thermal excess model that best fits the data shown in green. Applying thermal excess models that are a few Kelvin off has noticeably large effects at longer wavelengths, either causing an upturn or downturn of wavelengths longer than ~3.5 μm. Figure 6b shows the reflectance using different thermal models, with an optimum model at 251 K and models that are ± 5 and 10 K.

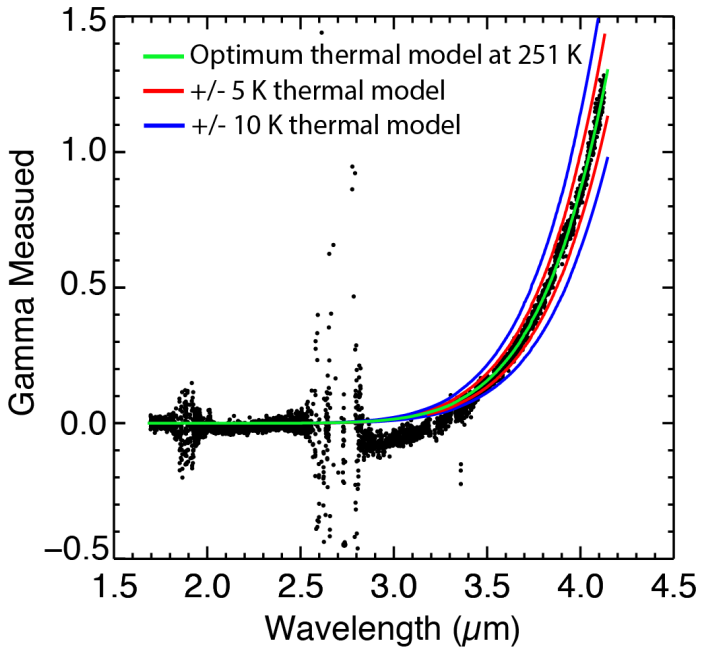

Figure 5: Example lunar thermal excess and the thermal excess model to be removed. Longer wavelengths constrain which thermal model is selected.

Once the appropriate thermal excess model has been found, we remove the optimum γ_{model} from our normalized continuum removed lunar spectra. We then scale the data to MI reflectance at the standard viewing geometry (i, e, phase, 30˚, 0˚, 30˚) and introduce the continuum back into the reflectance spectrum resulting in bidirectional reflectance at the photometric geometry of i = 30˚, e = 0˚, phase = 30˚ (Figure 6a):

$$R_{Moon} = MI_{30,0,30} * \left(\frac{\frac{R_{Moon}}{star}}{R_{con}} - \gamma_{model} \right) * R_{con}, \quad (8)$$

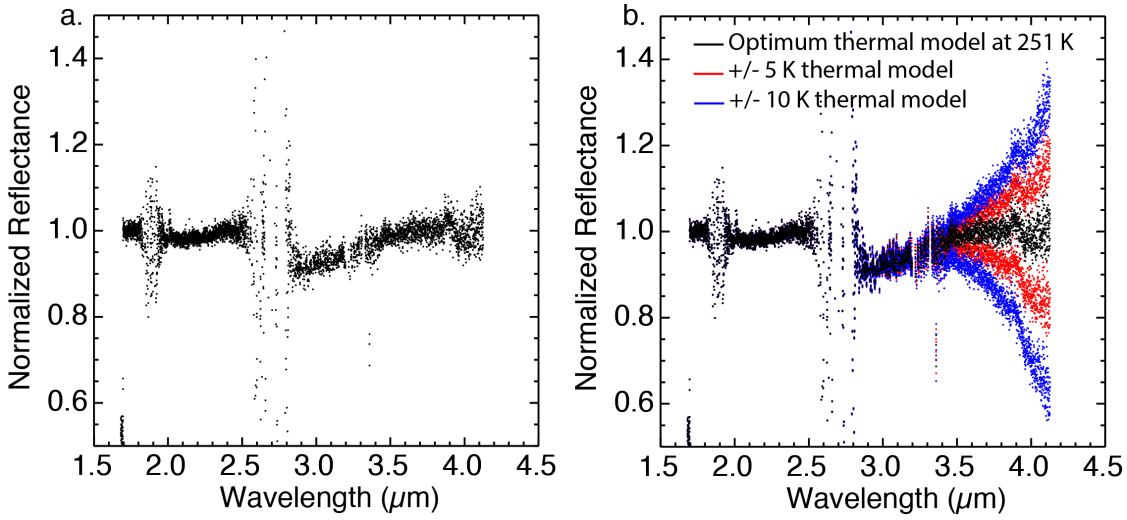

Figure 6: On left is an example of a lunar reflectance spectrum with a linear continuum removed and after the thermal emission has been corrected. On right is multiple thermal excess models removed that are ± 5 and 10 K from the optimum thermal model.

3.4 Estimating the Abundance of Total Water

The abundance of H_2O in geologic samples has been estimated for decades using the infrared absorption near 3 μm where the thickness of the sample is carefully measured, and use established absorption data for water and hydroxyl. Milliken and Mustard (2005) developed a relationship for estimating the abundance of H_2O in remote sensing data. Later, Li and Milliken (2017) applied this approach to the Moon using empirical measurements of water bearing glasses to calibrate M^3 data to water concentration. To estimate the abundance of total water we use the methods of the Li and Milliken (2017) that employs the spectral parameter, Effective Single Particle Absorption Thickness (ESPAT), that is linearly proportional to the abundance of total water.

ESPAT is a function of the single scattering albedo (*w*), which is the probability that a photon will survive an encounter with a grain. To calculate ESPAT from our reflectance data, we convert the reflectance spectra to *w* using work by Hapke (1981; 1993) (Li, 2017). We remove a continuum spectrum from the *w* spectra by fitting a straight line similar to the thermal excess process, but in *w* units. This differs from Li (2017) who used the *w* value at single wavelength (2.5 μm) and normalized the *w* spectrum to this value. The Li (2017) method does not take into account the inherently red lunar continuum, so with a single value as the continuum point it is possible to underestimate the continuum on the long wavelength shoulder of the 3 μm band causing negative abundances at low total water abundances. Fitting the SpeX data between 1.7 and 2.5 μm with care to avoid fitting the 2 μm pyroxene band provides a red continuum more appropriate for the Moon. This method reduces the occurrence of negative values when low abundances of total water are present providing a mean of zero. The continuum removed *w* is then used to calculate ESPAT:

$$ESPAT = \frac{1-w}{w} \quad (9)$$

Li and Milliken (2017) derived an empirical relationship to convert ESPAT to absolute total water content using a particle size of 60 to 80 μm. This particle range gives a conversion factor from ESPAT to wt.% of 0.5 (Figure 7a). However, Li and Milliken (2017) calculated this relationship at 2.86 μm, the maximum absorption of hydroxyl (Figure 7a) and is the standard wavelength for laboratory measurement of total water using FTIR data. This wavelength is within the opaque region of atmospheric transmission and therefore observations at this wavelength with

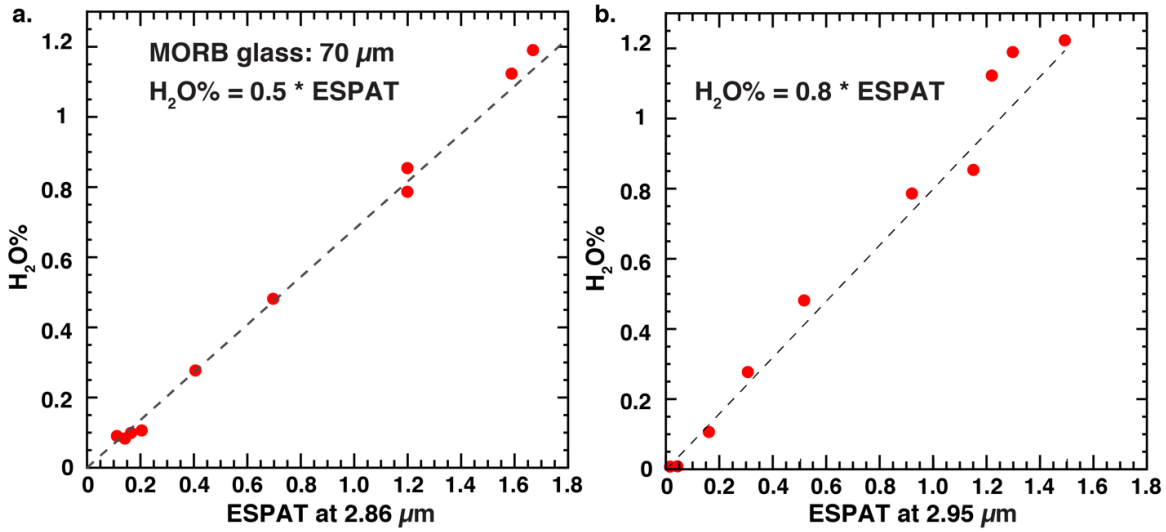

Figure 7: a) Empirical relationship between ESPAT and absolute content H_2O in water-bearing terrestrial glasses (Li, 2017) at wavelengths 2.86 μm. b) The same relationship except at 2.95 μm. We use the relationship for 2.95 μm because from the ground the 2.86 μm region is opaque.

the IRTF are not possible. For this reason we use the average value between 2.9 μm and 3 μm for the estimate of ESPAT of the 3 μm region. Instead of using 2.86 μm for the conversion of ESPAT to wt.%, we derive the empirical relationship at 2.95 μm providing a conversion factor of 0.8 (Figure 7b). After the calculation of ESPAT, we convert to total water abundance in ppm H_2O via:

$$H_2O\ ppm = 0.8 * ESPAT * 10000. \quad (9)$$

When the abundance of total water is low or zero, the ESPAT calculation sometimes results in negative numbers which is expected in the presence of noise.

4 Results

The presence of total water in our spectra is indicated by a clear discontinuity between 2.5 and 2.9 μm, similar to the "sharp 3 μm group" of Takir and Emery (2012) observed in some asteroid spectra. Figure 8 shows examples of 'wet' spectra and 'dry' spectra. In addition to the total water

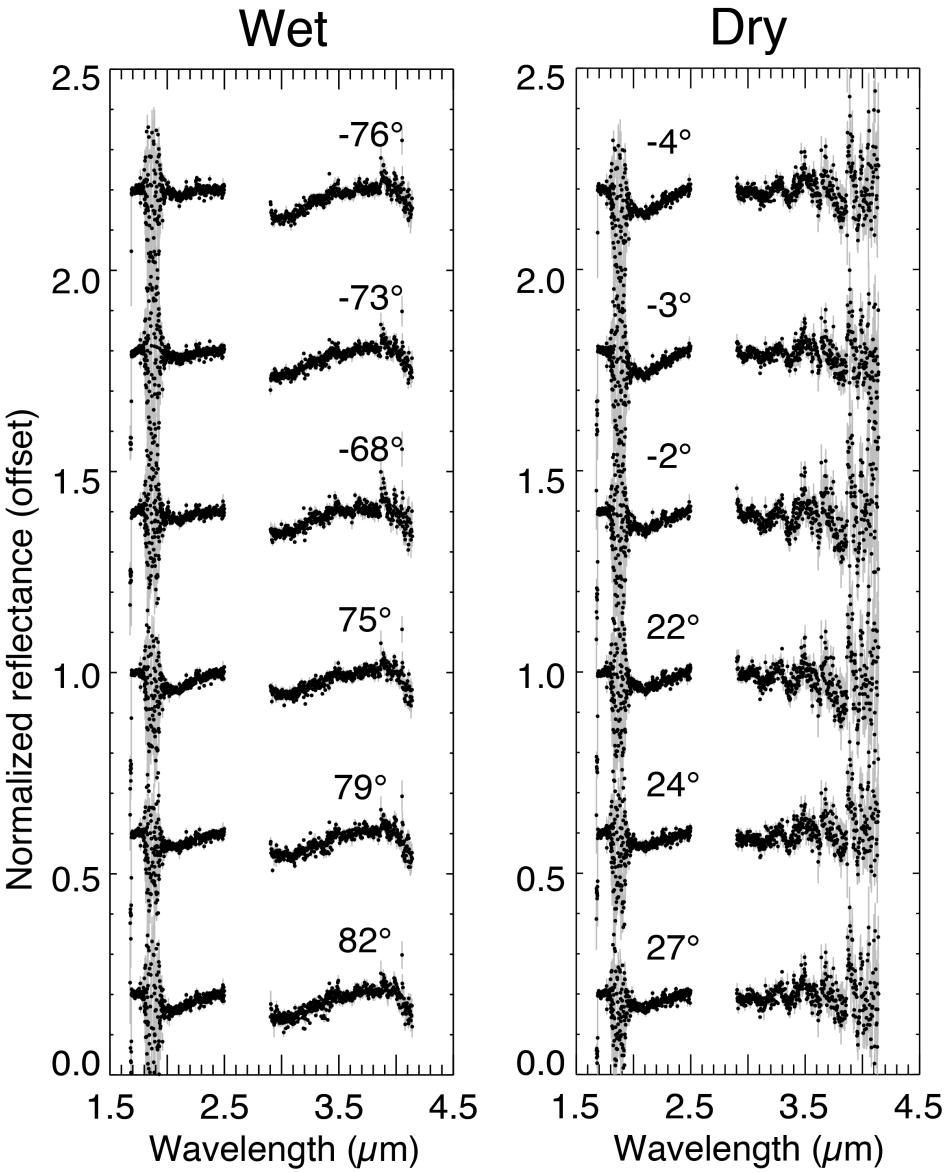

Figure 8: "Wet" and "dry" spectra from January 18th, 2019 observing run. The spectra show variations in strength and shape of the 3 μm band along with variations in the 2 μm pyroxene band.

feature, a pyroxene band is also observed at 2 μm in most spectra. Strong variations in depth of the 3 μm absorption are observed, and range from no absorption (Figure 8 right) to a strong 3 μm absorption (Figure 8 left). Most of the 'wet' spectra are found at higher latitudes while most of the 'dry' spectra are found at mid-latitudes and near the equator. The 'dry' spectra also show more noise at longer wavelengths compared to the 'wet' spectra. This is due to the large thermal emission component near the equator compared to the reflectance component. When removing the thermal excess model from the equatorial spectra we are removing a majority of the observed signal and looking at the lower reflectance signal which introduces noise at the thermally dominated longer wavelengths.

4.1 Diurnal variation

We calculated the total water abundance from all data collected and plot it as a function of lunar latitude and lunar time of day in Figure 9. The data are interpolated to have one spectrum per degree of latitude. The size of the points represent the abundance of total water; larger points indicate more total water while the smallest points have approximately zero ppm H_2O. For the sake of viewing diurnal effects, the abundances are limited to a maximum of 500 ppm (maximum abundances do not exceed 700 ppm H_2O). Along each observed chord, as a function of latitude, there are strong variations in total water concentrations. The minimum water observed occurs at low-northern latitudes at mid-morning to noon hours. Maxima for each chord occurs at high latitudes with increased abundances in the South compared to the North. Diurnal variations are seen across constant latitude in Figure 9. With increasing time of day the abundances decrease towards local noon. We lack data for the mid-afternoon, but the sunset data show the total water values have recovered. There is an asymmetric trend about the equator that favors the southern latitudes with higher total water abundances.

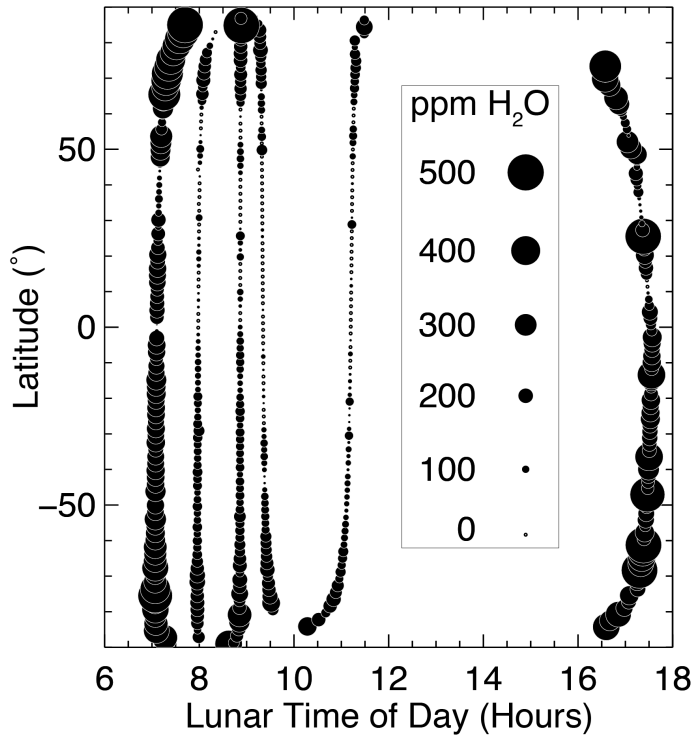

Figure 9: Estimated total water abundance of the observed pole-to-pole chords plotted as lunar time of day vs. latitude. Symbol size is proportional to the abundance of total water.

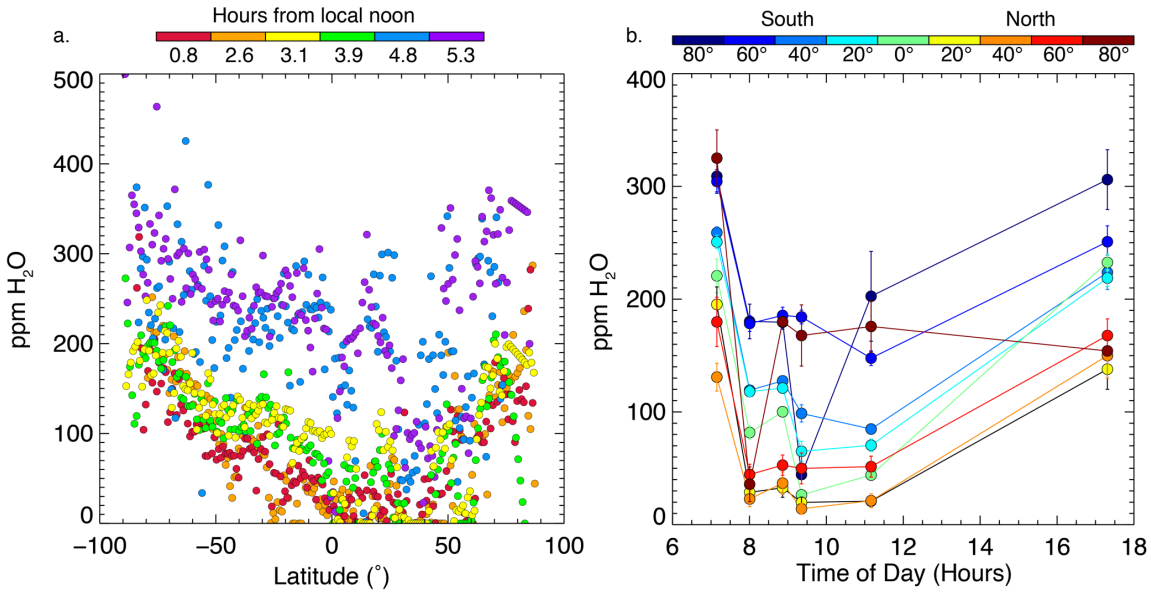

Figure 10: Variations of total water abundance in ppm H_2O plotted against latitude (a) and time of day (b) for the pole-to-pole observations.

Figure 10a plots the total water abundance versus latitude where each color represents a single pole-to-pole observation and its time from local noon. The two pole-to-pole observations that were acquired at the furthest time from local noon (near 07:00 (blue) and 17:00 (purple) hours) show the highest abundances across all latitudes with a weak latitude dependence. The four other pole-to-pole observations show a strong latitude dependence. A sharp drop from morning, 4.8 hours before local noon to 3.1 hours before local noon, is also seen in this plot. In Figure 10b, we plot the abundance of total water versus time of day where the color is proportional to proximity to the equator with brighter colors being closer to the equator and therefore hotter than the darker colors that are farther from the equator and colder. The latitudes were binned into 10° increments from 90°S to 90°N and the abundance within each 10° wide bin was averaged and plotted at their average time of day for each pole-to-pole observation. A sharp drop is observed at all latitudes from 07:00 to 08:00. After that, the abundance stays relatively constant at each latitude, except for an anomalous point for 80° – 90° N at ~09:00. At some point between local noon and late afternoon total water recovers close to the dawn values.

These plots show a strong diurnal variation at mid-southern latitudes, and a weaker but still present diurnal variation at low latitudes and mid-northern latitudes. The high latitudes also show a weak diurnal variation, but at later local times than at low- and mid-latitudes.

There is an asymmetry in abundance of total water with the northern latitudes having less total water than the southern latitudes (Figure 9 and 11). The asymmetry may be influenced by mare versus highland materials. Figure 11 shows the diurnal plot from Figure 9 with the highland material colored black and the mare material colored red. Mare is only observed at northern latitudes possibly explaining the asymmetry in total water between the north and south. However, the effects of composition are expected to small compared to the effects of latitude and lunar time of day. This is expected because where mare was observed, the highland material observed nearby has similar abundances of total water.

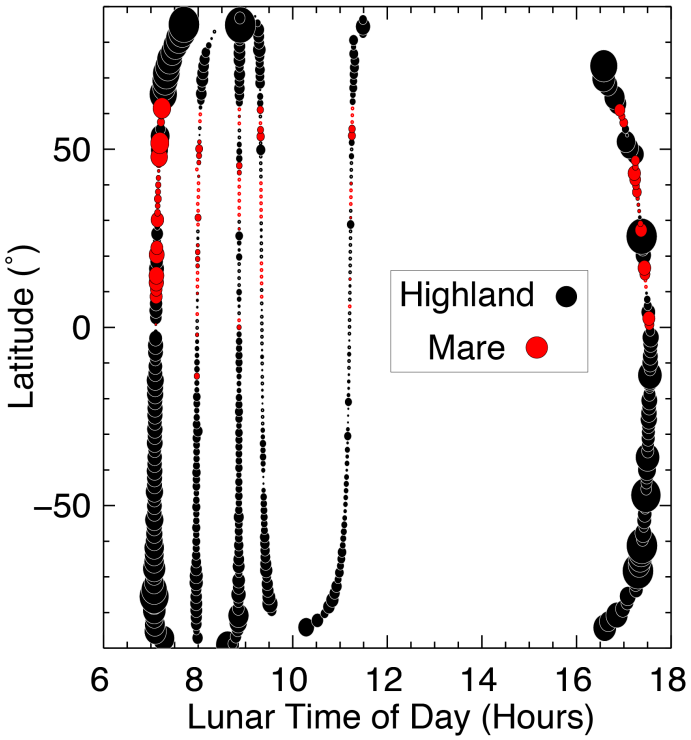

Figure 11: Mare vs. Highland pole-to-pole chords plotted as lunar time of day vs. latitude. Red points indicated mare compositions while black indicates highland compositions. Symbol size is proportional to the abundance of total water.

5 Discussion

In our lunar spectra, corrected using the strong constraint of thermal wavelengths, we observe variations in the 3 µm hydration band depth and derived water content with latitude, time of day, and composition. This result is in agreement with a number of studies (Sunshine et al., 2006; Li and Milliken, 2017; Wöhler et al., 2017; Grumpe et al., 2019), which also observe variations in the 3 µm band in spacecraft data. The variation indicates that the species responsible for the 3 µm band are undergoing temperature driven processes.

The observed diurnal variations are largely in agreement with Li and Milliken (2017), but with some differences. First, the total water abundances we measure are lower than those of Li and Milliken (2017) by a factor of about 1.5. This difference could be due to the uncertainty in removing thermal emission from M^3 data unconstrained by thermally dominated wavelengths near 4 µm.

The second difference is our observed asymmetry between the northern and southern hemispheres. Li and Milliken (2017) observe higher abundances in the northern hemisphere while we observe higher abundances in the southern hemisphere. One possible explanation for this is the lunar time of day at which the M^3 observations were acquired. The M^3 southern observations were taken slightly closer to lunar noon than the northern observations, possibly creating the asymmetry seen in M^3 data. The asymmetry in our data cannot be explained by a difference in acquisition times. Another possible source for the observed asymmetry is composition. Across our pole-to-pole scan we traverse through mare and highland regions with most of our northern observations in mare regions and our southern observation in highland regions. Our results agree with Wöhler

et al. (2017) and McCord et al. (2011) that highland material retains more total water than mare material.

Due to the lack of data in the lunar mid-afternoon, we cannot comment on the symmetry of abundance between dawn and dusk terminators, but we do note that abundances at 07:00 and 17:00 are similar. This is in contrast to Li and Milliken (2017) who report more total water in the morning than in the afternoon. Again, this could be due to the time of day the data was acquired with M^3, with the afternoon observations begin closer to noon than the morning observations. We are, however, in agreement with Wöhler et al. (2017) and Grumpe et al. (2019) who see similar abundances between morning and afternoon using their version of thermally corrected M^3 data. Wöhler et al. (2017) and Grumpe et al. (2019) did not provide estimates of total water in absolute concentrations and so we cannot directly compare our abundances to their results.

There are two models that have sought to explain previously reported diurnal variations. The first is that the variation is due to H_2O migrating along temperature gradients (Sunshine et al., 2009; Hendrix et al., 2012; Hendrix et al., 2019) and the second that it is due to metastable OH forming during the process of solar wind H diffusing through the regolith (Tucker et al., 2019, Farrell et al., 2017, Starukhina, 2006). Hendrix et al., (2019) observed a diurnal variation in the far ultra-violet (FUV) water ice band ratio using Lyman Alpha Mapping Project (LAMP) data. They show a sudden drop in the FUV ratio intensity near lunar noon that they attribute to a release of molecular water that is bound to the surface with relatively high activation energy. This stands in contrast with our data that show a sudden spectral change in the early morning. If our observed signal is due to molecular water, then the activation energy that binds the water to the surface would be low. The FUV and infrared do sample the surface differently; at FUV wavelengths lunar surface particles are highly opaque and spectral changes must be confined to the grain surfaces. In contrast, at 3 μm particles are relatively transparent and the reflectance signal can arise from the volume of the particle, and several grains deep within the surface. However, it is difficult to envision how water could exchange with the grain interior over diurnal timescales, so in effect the infrared signal must be a surface phenomenon if due to water. If migrating water is the source of the spectral variations in the FUV and infrared, the two data sets are inconsistent in their timing during the diurnal cycle.

An additional issue with the hypothesis that molecular water can account for the diurnal variations is that it implies large amounts of water supplied to the lunar exosphere on a diurnal basis; something not measured by the Lunar Atmosphere Dust and Environment Explorer (LADEE). Hendrix et al. (2019) noted that their analysis suggested a few hundred particles per cubic centimeter at the altitude of the LADEE spacecraft. LADEE, however, measured water in the exosphere on the order of tens of particles per cubic cm or less (Benna et al., 2019). Scaling to calculations from Farrell et al. (2019), the water release rate from the abundance we measure at 3 μm would yield 10^{10} water molecules per cubic centimeter, ten orders of magnitude higher than the LADEE maximum detection.

Both our data and the FUV data are ambiguous with respect to H_2O vs. OH. Tucker et al. (2019) investigated the alternate process that the infrared signal was due to temperature dependent formation and destruction of metastable hydroxyl as solar wind hydrogen migrates through the optical surface. They found that the model abundances of hydroxyl could roughly account for the infrared signal published by Li and Milliken (2017) which are roughly consistent with our study. This hypothesis does not resolve the inconsistencies between the FUV and our infrared results, but metastable temperature-dependent hydroxyl is more consistent with the exospheric constraints than migrating H_2O.

Finally, our observation of a latitude dependent hydration signal that persists even at local noon is consistent with the presence of stable hydroxyl. Hydroxyl at the ~100 ppm level has been found in lunar impact glasses sampled at the equator by Apollo (Liu et al., 2012), and averaged over the lunar soil which contains about 70% nominally anhydrous minerals (McKay et al., 1991) would be equivalent to about 30 ppm, roughly consistent with our results. The increase with latitude is consistent with the model of Jones et al. (2019) that showed that equatorial hydroxyl would tend to be depleted by associative desorption of water and that hydroxyl would steadily increase with latitude, but not exhibit a diurnal signal. Our observations are best explained by a combination of metastable hydroxyl that accounts for the diurnal signal, and stable hydroxyl that accounts for the latitude dependence.

6 Conclusions

Using data constrained by thermally dominated wavelengths, we have applied published methods for reducing spectra of asteroids to produce thermally corrected spectra of the lunar surface in the 3 μm region. Using pole-to-pole data scans along the 0 longitude meridian obtained at several lunar times of day, we find that a 3 μm hydrous absorption feature is widespread on the lunar surface, and its intensity shows strong variations with latitude, lunar time of day, and composition. The observed diurnal variations are most consistent with a model of diurnally evolving metastable hydroxyl. Attributing the signal to molecular water implies much more water in the exosphere than has been measured in lunar orbit by the LADEE spacecraft. Latitude variations superimposed on the diurnal signal are consistent with the presence of stable hydroxyl that has been found in lunar impact glasses. The latitude dependence is explained by a temperature dependent depletion of hydroxyl by associative desorption of water over much longer timescales than the lunar diurnal cycle.

Acknowledgments and Data

Visiting Astronomer at the Infrared Telescope Facility, which is operated by the University of Hawaii under contract NNH14CK55B with the National Aeronautics and Space Administration. All raw data are available on the NASA/IPC Infrared Science Archive (https://irsa.ipac.caltech.edu/applications/irtf/)18 months after the date listed in Table 1 and the file names of data used in this project are provided in the Supplement in Table S1. Prior to this we will make the data available on a temporary site at the University of Hawai‘i at Mānoa.

References

Arnold, J. R. (1979). Ice in the lunar polar regions. *Journal of Geophysical Research: Solid Earth (1978–2012)*, *84*(B10), 5659-5668.

Bandfield, J. L., Hayne, P. O., Williams, J.-P., Greenhagen, B. T., & Paige, D. A. (2015). Lunar surface roughness derived from LRO Diviner Radiometer observations. Icarus, 248, 357–372.

Bandfield, J. L., Poston, M. J., Klima, R. L., & Edwards, C. S. (2018). Widespread distribution of OH/H 2 O on the lunar surface inferred from spectral data. *Nature Geoscience*, 11(3), 173–177.

Benna, M., Hurley, D.M., Stubbs, T.J., Mahaffy, P.R., Elphic, R.C. Lunar soil hydration constrained by exospheric water liberated by meteoroid impacts. Nature Geoscience. 12, 333 (2019).

Clark, R. N. (2009). Detection of Adsorbed Water and Hydroxyl on the Moon. *Science*, *326*(5952), 562-564.

Cushing, M. C., Vacca, W. D., & Rayner, J. T. (2004). SpeXtool: A Spectral Extraction Package for SpeX, a 0.8–5.5 Mm Cross-Dispersed Spectrograph. Publications of the Astronomical Society of the Pacific, 116(818), 362–376.

Farrell, W. M., Hurley, D. M., Esposito, V. J., McLain, J. L., & Zimmerman, M. I. (2017). The statistical mechanics of solar wind hydroxylation at the Moon, within lunar magnetic anomalies, and at Phobos. *Journal of Geophysical Research: Planets*, 122(1), 269–289.

Gruen, D.M., Wright, R.B., McBeth, R.L., Sheft, I. (1975). Hydroxyl formation accompanying defect center production in proton and deuteron bombarded aluminum oxide. J. Chem. Phys. 62 (3), 1192–1193.

Grumpe, A., Wöhler, C., Berezhnoy, A. A., & Shevchenko, V. V. (2019). Time-of-day-dependent behavior of surficial lunar hydroxyl/water: Observations and modeling. *Icarus*, 321, 486–507.

Guermazi, M., Thevenard, P., Brenier, R. (1987). Ion implantation effects in TiO_2 bombarded with protons and deuterons. Nucl. Instrum. Methods Phys. Res. B19/20, 912–916.

Harris, A.W., 1998. A thermal model for near-Earth asteroids. Icarus 131, 291–301.

Hapke, B. (1965), Effects of a simulated solar wind on the photometric properties of rocks and powders. *Ann. NY Acad. Sci. 123*, 711–721.

Hapke, B. (2012). Theory of Reflectance and Emittance Spectroscopy. Cambridge Univ. Press.

Hendrix, A. R., Hurley, D. M., Farrell, W. M., Greenhagen, B. T., Hayne, P. O., Retherford, K. D., et al. (2019). Diurnally Migrating Lunar Water: Evidence From Ultraviolet Data. *Geophysical Research Letters*, 46(5), 2417–2424.

Hibbitts, C. A., G. A. Grieves, M. J. Poston, M. D. Dyar, A. B. Alexandrov, M. A. Johnson, and T. M. Orlando. (2011). Thermal stability of water and hydroxyl on the surface of the Moon from temperature-programmed desorption measurements of lunar analog materials, *Icarus*, *213*(1), 64-72.

Ichimura, A. S., Zent, A. P., Quinn, R. C., Sanchez, M. R., & Taylor, L. A. (2012). Hydroxyl (OH) production on airless planetary bodies: Evidence from H+/D+ ion-beam experiments. *Earth and Planetary Science Letters,* 345-348, 90–94.

King, P. L., McMillan, P. F., and Moore, G. M. (2004). Chapter 4. Infrared Spectroscopy Of Silicate Glasses With Application To Natural Systems. *Mineralogical Association of Canada*, 93–134.

Lebofsky, L. A. (1978). Asteroid 1 Ceres: evidence for water of hydration. Mon. Not. R. Astr. Soc., 182, 17–21.

Lebofsky, L. A., et al. (1986). A Refined 'Standard' Thermal Model for Asteroids Based on Observations of 1 Ceres and 2 Pallas. *Icarus*, 68(2), 239–251., doi:10.1016/0019-1035(86)90021-7.

Li, S. (2017). Water on the Lunar Surface as Seen by the Moon Mineralogy Mapper: Distribution, Abundance, and Origins. *Brown University,* PhD Dissertation (pp. 1–311).

Li, S. & Milliken, R. E. (2017). Water on the surface of the Moon as seen by the Moon Mineralogy Mapper: Distribution, abundance, and origins. *Science Advances*, 3(9), e1701471.

Liu, Y. et al. Direct measurement of hydroxyl in the lunar regolith and the origin of lunar surface water. Nature Geoscience, 5, 779-782 (2012).

Mattern, P.L., Thomas, G.J., Bauer, W., 1976. Hydrogen and helium implantation in vitreous silica. J. Vac. Sci. Technol. 13 (1), 430–436.

McCord, T. B., Taylor, L. A., Combe, J. P., Kramer, G., Pieters, C. M., Sunshine, J. M., & Clark, R. N. (2011). Sources and physical processes responsible for OH/H2O in the lunar soil as revealed by the Moon Mineralogy Mapper (M3). *Journal of Geophysical Research: Planets*, *116*, 1–22.

McIntosh, I. M., Nichols, A. R. L., Tani, K., and Llewellin, E. W. (2017). Accounting for the species-dependence of the 3500 cm^{-1} H_2O infrared molar absorptivity coefficient: Implications for hydrated volcanic glasses. *American Mineralogist*, 102, 8, 1677–1689.

McKay, D. S. et al. in Lunar Sourcebook (eds Heiken, G., Vaniman, D. & French, B.) (Cambridge Univ. Press, 1991).

Milliken, R. E. And Li, S. (2017). Remote detection of widespread indigenous water in lunar pyroclastic deposits. *Nature Geoscience,* 10, 561-565.

Milliken, R. E. and Mustard, J. F. (2005). Quantifying absolute water content of minerals using near-infrared reflectance spectroscopy. *Journal of Geophysical Research.* 110, E12001, 1-25.

Ohtake, M. et al. (2008). Performance and scientific objectives of the SELENE (KAGUYA) Multiband Imager. *Earth Planet Space*, 60, 257-264.

Pieters, C. M., Goswami, J. N., Clark, R. N., Annadurai, M., Boardman, J., Buratti, B., et al. (2009). Character and Spatial Distribution of OH/H2O on the Surface of the Moon Seen by M3 on Chandrayaan-1. *Science*, 326(5952), 568–572.

Rayner, J. T., Toomey, D. W., Onaka, P. M., Denault, A. J., Stahlberger, W. E., Watanabe, D. Y., & Wang, S.-I. (2003). SpeX: A Medium-Resolution 0.8-5.5 micron Spectrograph and Imager for the NASA Infrared Telescope Facility. PASP, 115, 362.

Reddy, V., Emery, J.P., Gaffey, M.J., Bottke, W.F., Cramer, A., Kelley, M.S., 2009. Composition of 298 Baptistina: Implications for the K/T impactor link. *Meteor. Planet. Sci.* 44, 1917–1927.

Rivkin, A., Binzel, R., and Bus, S. (2005). Constraining near-Earth object albedos using near-infrared spectroscopy. Icarus, 175(1), 175–180.

Siskind, B., Gruen, D.M., Varma, R. (1977). Chemical implantation of 10-keV H^+ and D^+ in rutile. *J. Vac. Sci. Technol.* 14, 537–542.

Starukhina, L. (2001). Water detection on atmosphereless celestial bodies: Alternative explanations of the observations. Journal of Geophysical Research, 106, 701–710.

Starukhina, L. V. (2006). Polar regions of the moon as a potential repository of solar-wind-implanted gases. *Advances in Space Research*, 37(1), 50–58.

Stolper, E. (1982). Water in silicate glasses: An infrared spectroscopic study. *Contributions to Mineralogy and Petrology*, 81, 1–17.

Sunshine, J. M., Farnham, T. L., Feaga, L. M., Groussin, O., Merlin, F., Milliken, R. E., & A'Hearn, M. F. (2009). Temporal and Spatial Variability of Lunar Hydration As Observed by the Deep Impact Spacecraft. *Science*, 326(5952), 565–568.

Takir, D., & Emery, J. P. (2012). Outer Main Belt asteroids: Identification and distribution of four 3-μm spectral groups. Icarus, 219(2), 641–654.

Tucker, O. J., Farrell, W. M., Killen, R. M., & Hurley, D. M. (2019). Solar Wind Implantation Into the Lunar Regolith: Monte Carlo Simulations of H Retention in a Surface With Defects and the H2 Exosphere. *Journal of Geophysical Research: Planets*, 124(2), 278–293.

Vacca W. D., Cushing M. C., & Rayner J. T. (2003), A Method of Correcting Near-Infrared Spectra for Telluric Absorption, PASP 115, 389.

Watson, K., B. C. Murray, and H. Brown (1961), The behavior of volatiles on the lunar surface, *Journal of Geophysical Research*, *66*(9), 3033-3045.

Wöhler, C., Grumpe, A., Berezhnoy, A. A., & Shevchenko, V. V. (2017). Time-of-day–dependent global distribution of lunar surficial water/hydroxyl. *Science Advances*, 3(9).

Zeller, E. J., & Ronca, L. B. (1967). Space weathering of lunar and asteroidal surfaces. *Icarus*, 7(1-3), 372–379.

Zeller, E.J., Ronca, L.B., Levy, P.W. (1966). Proton-induced hydroxyl formation on the lunar surface. *J. Geophys. Res.* 71, 4855–4860.